Ultramicroscopy 160 (2016) 130–139

Contents lists available at ScienceDirect

Ultramicroscopy

journal homepage: www.elsevier.com/locate/ultramic

Quantitative nanoscopy: Tackling sampling limitations in (S)TEM imaging of polymers and composites

Karthikeyan Gnanasekaran, Roderick Snel, Gijsbertus de With *, Heiner Friedrich

Laboratory of Materials and Interface Chemistry, Department of Chemical Engineering and Chemistry, Eindhoven University of Technology, Eindhoven, The Netherlands

ARTICLE INFO

Article history:
Received 7 May 2015
Received in revised form
28 September 2015
Accepted 6 October 2015

Keywords:
Automatic image acquisition and stitching
Large-scale image analysis
Polymer materials
Quantitative image analysis
Sampling limitation
(scanning) Transmission electron microscopy.

ABSTRACT

Sampling limitations in electron microscopy questions whether the analysis of a bulk material is representative, especially while analyzing hierarchical morphologies that extend over multiple length scales. We tackled this problem by automatically acquiring a large series of partially overlapping (S)TEM images with sufficient resolution, subsequently stitched together to generate a large-area map using an in-house developed acquisition toolbox (*TU/e Acquisition ToolBox*) and stitching module (*TU/e Stitcher*). In addition, we show that quantitative image analysis of the large scale maps provides representative information that can be related to the synthesis and process conditions of hierarchical materials, which moves electron microscopy analysis towards becoming a bulk characterization tool. We demonstrate the power of such an analysis by examining two different multi-phase materials that are structured over multiple length scales.

1. Introduction

Polymer composites have a broad range of applications from simple commodity plastics (e.g., cups, bottles, food packaging) to high-end materials (e.g., strong but light weight aviation and aerospace structures, EM-shielding and biomedical coatings). To tailor the (macroscopic) functional properties of polymer composites, a proper understanding on how the nanoscopic morphology translates into function over multiple length scales is required. Especially in multiphase polymer blends and polymer/particle composites, a hierarchical morphology is often introduced by processing [1,2], which extends from the nanometer scale (e.g., size and arrangement of crystalline lamella, nanoparticles) via the micrometer scale (phase separation into domains, homogeneity) to the macroscale (mechanical strength, functional and surface properties). Hence, a bottom-up multiscale characterization and analysis of the resulting hierarchical structures is essential for improving processing conditions and for designing novel materials and devices.

Morphologies of organic, inorganic or hybrid materials can be analyzed by scattering and microscopic techniques, like X-ray scattering (WAXS and SAXS), SEM, FIB–SEM, (S)TEM, AFM and tomography. All these techniques have their own niches and limitations, particularly for analyzing multiscale morphologies on millimeter scale with nanometer resolution. Though scattering analysis can probe large volumes with nanometer resolution, local analysis of any particular features, like phase separation, agglomeration, orientation distribution, pore size distribution and volume fraction distribution is difficult and features are hard to distinguish in the, basically unknown, overall morphology, as the information is clouded by overall averaged information. Imaging techniques provide a more intuitive representation of the morphology and allows for the analysis of specific features. Besides that, imaging provides directly a model for complicated morphologies that can be used in scattering analysis [3,4]. Imaging techniques like X-ray mapping, SEM, and FIB–SEM provide an excellent platform for surface as well as bulk analysis of morphologies at the mesoscale; however, these techniques are usually limited by resolution down to few tens of nanometers due to their larger probe size compared to (S)TEM. Despite (Scanning) Transmission Electron Microscopy ((S)TEM) can provide structural information with nanometer resolution [5,6], it mainly deals with the morphologies from the micrometer scale down to the nanometer level [7,8]. This fact is often referred to as the sampling limitation in TEM while analyzing multiscale morphologies [9,10] and may lead to erroneous or subjective interpretations of images just depending on the chosen area, especially for heterogeneous and hierarchically ordered multiphase materials.

* Corresponding author.
E-mail address: G.deWith@tue.nl (G. de With).

http://dx.doi.org/10.1016/j.ultramic.2015.10.004
0304-3991/

2. (S)TEM sampling limitations

Due to the limited size of (S)TEM images, one can either decide to image at low magnification with a relatively large field of view at the cost of resolution or at high magnification with high-resolution, thus reducing the imaged area to below 10^{-12} m^2. Hence in conventional practice, for capturing the morphology of complex materials, several high-resolution images are acquired at various regions of the sample supported by low magnification and low-resolution overviews (Fig. 1a–c). By doing so, the entire morphology can be assessed visually, but connectivity and continuity from one region to another, including quantification, is not obtainable. This sheds some doubts on the validity of the conclusions derived from a few TEM images (Fig. 1b and c) for the analysis of hierarchical systems over multiple length scales.

Multi-scale imaging of hierarchical materials is even more faceted as one rather needs to look from the point of view of imaging for a representative volume element, i.e., the smallest volume over which a measurement can be made that will yield a value representative of the bulk material. Imaging of representative volumes can be split up into two contributions: (1) imaging large-areas and (2) combined with as thick as possible sections to make the process efficient. However, Bright-Field (BF)-TEM is not the most suitable imaging mode for thick sections. In BF-TEM the signal-to-noise ratio (SNR) decreases considerably with increasing section thickness (Fig. 1d). This eventually results in such low contrast that interpretation and quantification becomes unfeasible. Scanning transmission electron microscopy (STEM) has shown potential to image thick samples (Fig. 1e and f) with nanometer resolution and with good contrast between phases [11]. Following previous studies by Aoyama et al. [12], Motoki et al. [13], Loos et al. [14], and in our experience images of thick sections of polymers and composites are best acquired in STEM mode using a high acceleration voltage (in our case 300 kV) and by choosing an optimum balance between the probe convergence angle, the desired resolution and the camera length which might vary between samples.

The solution to overcome the sampling limitation is to record images sequentially with a small overlap between the images and stitch them together to achieve a large area map. Depending on the material to be analyzed, the required field of view to record representative information can be potentially extended to the entire TEM grid. Manual data collection and stitching of such a huge number of images is impractical, which triggered us to automate the entire process for STEM (and TEM) imaging.

Microscope automation is a well-developed technique, especially in the field of biology and many (S)TEM automation software packages are available for various applications including: automatic tilt series acquisition in electron tomography (TOM Toolbox [15], SerialEM [16], UCSF Leginon [17], EM-TOMO, emScope [18]), automatic single particle acquisition (Auto-EM [19], EM-SPC, Xplore3D (FEI)). Along with these, some large-area EM data acquisition software are also available [10,15,16,20–22]; nevertheless, there is a lack of a STEM large area-acquisition toolbox, e.g., for polymers and composites research.

Hence, we implemented a (S)TEM automation package for recording, stitching and quantification of ultra-large (S)TEM maps. In the following sections automation of data acquisition (Section 3), alignment and stitching (Section 4), quantification by image analysis (Section 5) and applications to analysis of assemblies of carbon nanotubes in a polymer latex (Section 6) and multi-layer co-extruded polymer tapes (Section 7) will be discussed.

3. Automated image acquisition

Automatic image acquisition in both STEM and TEM mode was implemented on our TU/e CryoTitan by utilizing the TEM scripting

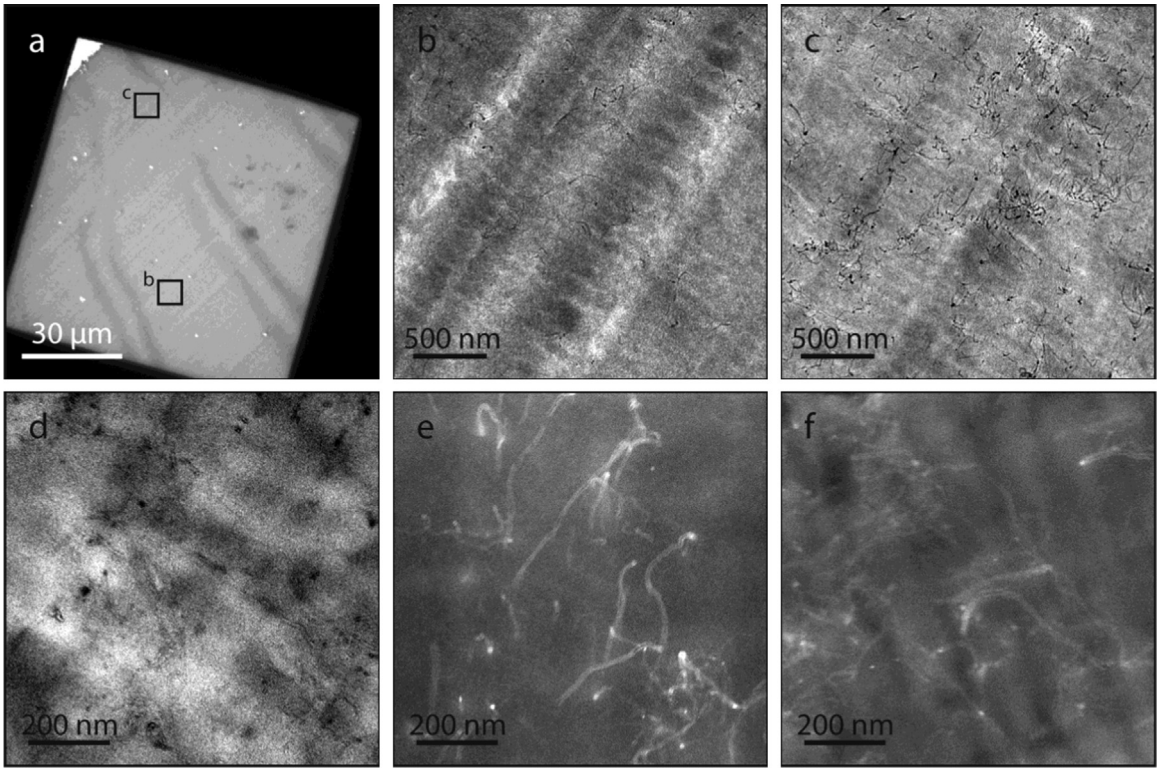

Fig. 1. (a) TEM overview of a polymer nanocomposite (PSPPO/MWCNT); (b, c) BF-TEM image illustrating the variation in the network morphology between different regions; (d) BF-TEM image of 500 nm thick section poor SNR and contrast. Image was acquired with defocus of −5 µm; (e) STEM image of 500 nm thick section showing significantly higher contrast); (f) STEM image of 1 µm thick section still showing good contrast and SNR.

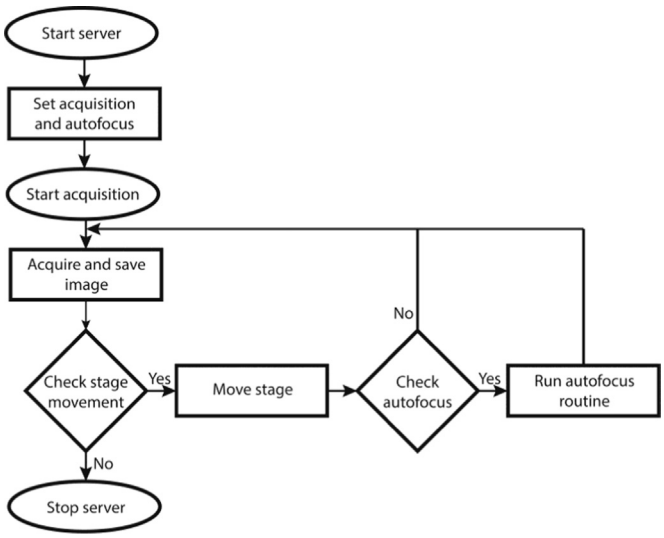

Fig. 2. Flowchart illustrating the process of acquiring and storing images in the TU/e Acquisition ToolBox.

component of the FEI microscope software, which enables the communication between a client script and the EM (See Supporting information, SI, Figure S1). An outline of the automatic acquisition workflow is displayed in Fig. 2. We used Python 2.7.2 version as scripting language because of its extensive range of available libraries and packages. PyInstaller and pyWin32 were used to create an executable and to create a COM connection with the TEM scripting interface, respectively. NumPy and SciPy libraries were used for mathematical operations such as automated focus correction. To prevent any breakdown in communication between the client script and the TEM scripting interface, we implemented operations in several threads. During data acquisition the microscope stage follows a serpentine movement to prevent excessive backlash between subsequent positions (see arrows in Fig. 3). Besides that, to prevent shakedown, an optimum time delay is given between the end of each stage movement and the beginning of each image acquisition. Acquisition parameters, such as dwell time, image size, autofocus settings and saving formats, can be set and controlled by a web-based graphical user interface (GUI) constructed in JavaScript (angularJS). A local web server for the GUI was developed on a Flask framework, which communicates via webSockets. Details on the autofocussing procedure and a screenshot of the GUI can be found in the SI, Section II. We denote the complete software package as the *TU/e Acquisition ToolBox*.

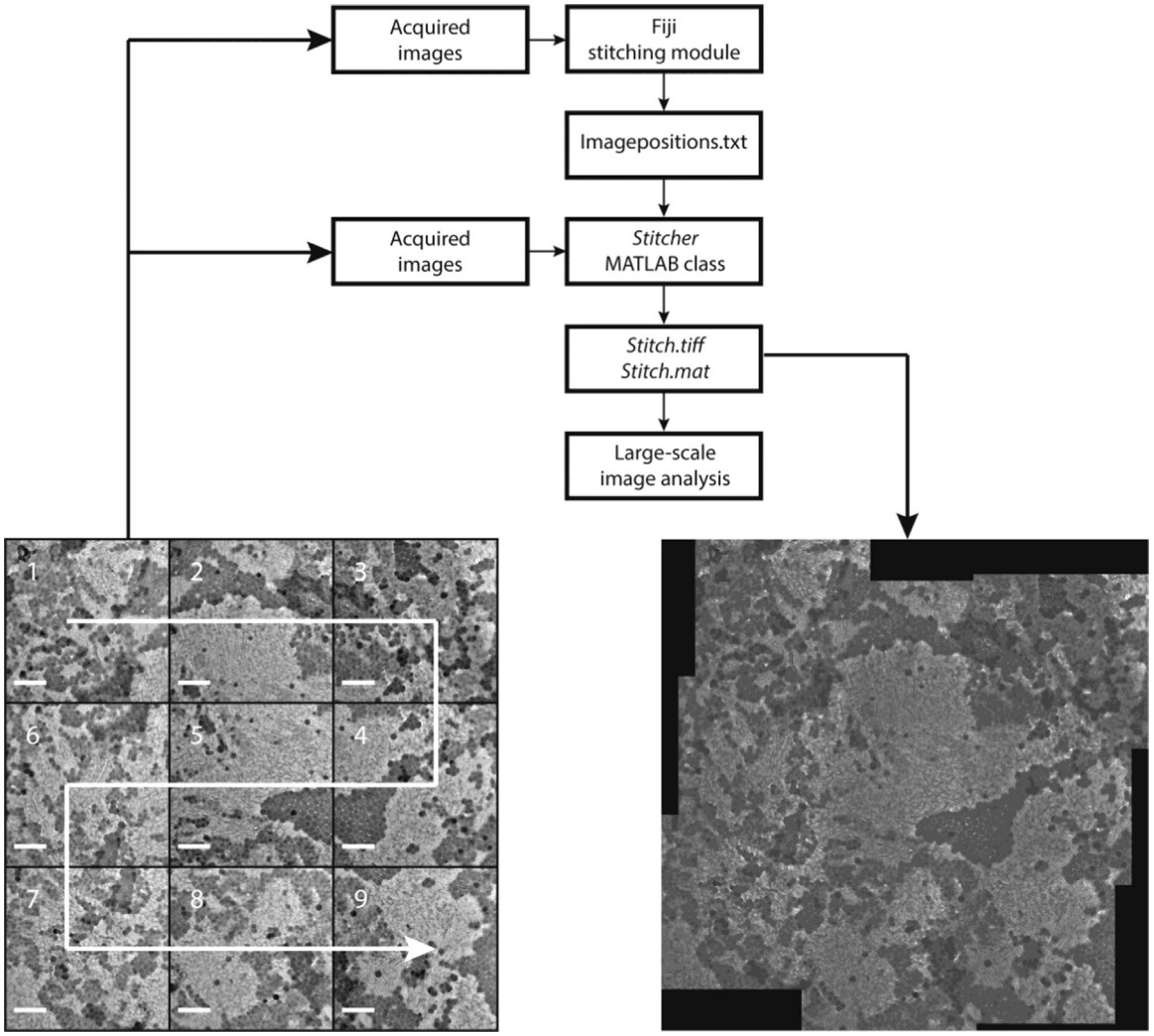

Fig. 3. Schematic of the stitching procedure to obtain a unified large-area map from individual images. White arrow represents the serpentine movement of stage to prevent excessive backlash. Scale bars are 500 nm.

4. Stitching

For a complete analysis and quantification of the acquired data, the individual images need to be stitched together to generate a single ultra-large EM map. Handy stitching applications are already available in software such as Adobe Photoshop, Autostitch and stitching plugin in Fiji (ImageJ). The stitching plugin in Fiji is a well-known stitching tool widely used, also for stitching EM images [23,24], and we decided to extend its applicable range, as the standard Fiji implementation is limited to a 4 GB file size. In brief, the Fiji stitching algorithm computes the normalized cross correlation co-efficient in the overlap areas of subsequent image pairs to calculate the final image shifts in the entire dataset. This list of shifts or offsets between the individual images is then exported in text format. In addition one can also export the completely stitched data (if <4 GB) to standard image formats like tiff, png, etc. More details on the workflow of the Fiji's stitching algorithm are given in the SI, Section III. Due to restrictions of the maximum file size to 4 GB, exporting data in TIFF fails during fusing images that contain more than 44720^2 pixels (5th step in SI, Section III). In addition, the algorithm also fails for the datasets that contain more than ≈ 625 images, possibly due to a memory size restriction on JAVA variables (4th step in SI, Section III). The 4 GB file size limit is overcome using our custom MATLAB script *TU/e Stitcher* that uses the image shift positions calculated by Fiji as the input data to compile the raw data of the complete field of view into a unified matrix (image) that is saved as a single MATLAB (.mat) file. This data file can be easily handled by MATLAB on a workstation with sufficient RAM (192 GB in our case) for further processing (e.g., structural quantification by image analysis) and for exporting to any standard image formats like tiff, png, etc. A schematic of the stitching process and an example are shown in Fig. 3.

To minimize the processing time, even for very large datasets, the data are split into several parts so that the stitching process can be carried out in parallel. For exporting the stitched data to tiff format, each part can only be set to a maximum size of 44720^2 pixels (≈ 4 GB) due to standard tiff limitation. For better handling of memory while stitching very large images, we use 16-bit integer data types (rather than standard MATLAB double data type), which results in a 4 times improvement in speed. To minimize artifacts from sample preparation (varying section thickness), acquisition (alignment and stability over long periods) and stitching (overlap between images), optional functions such as non-uniform background correction, non-linear blending and grid corrections are included. Detailed discussions of these functions can be found in the SI, Section IV–VI.

5. Quantification by image analysis

Besides qualitative assessments of the data by visual inspection, quantification of sample morphologies is becoming increasingly important in materials science. Quantification of structural properties is essential as, e.g., the volume fraction of components [8], the pore size distribution [25] or the orientation of features [26], all relate to the synthesis and processing conditions [27,28]. Moreover, any quantitative analysis is significantly influenced by the sampled volume (sampling limitation) and conclusive information can only be obtained by analyzing a representative volume. Hence, quantification of large-scale (S)TEM maps of hierarchical materials, as, e.g., generated by the *TU/e Acquisition ToolBox* and *Stitcher,* could emerge as an extension of (S)TEM towards the study of macroscopic sample properties. The required quantification is specific for each sample, but in general quantification is often based on thresholding to distinguish between different components in the sample. In the following we illustrated the versatility and power of quantitative nanoscopy on two examples: (1) assemblies of spin-coated, polymer latex-carbon nanotubes mixtures (Section 6) and (2) co-extruded multilayer polymer tapes (Section 7).

6. Spin-coated polymer latex-carbon nanotube composite

The deposition by spin-coating of a polymer latex/carbon nanotube (CNT) composite is investigated, as this material has a high potential for transparent electrodes in sensors and solar cells. The mutual interactions of the polymer latex particles and the carbon nanotubes, their size and size distributions significantly influence the morphology of the deposited CNT network, which in turn controls the macroscopic functional properties, i.e., the electrical conductivity [29–31]. In addition to that, deposition conditions, such as spin-coating speed or temperature, are also known to influence the final electrical conductivity [32,33]. Here we specifically analyze the preferential orientation of single-walled carbon nanotube assemblies (SWCNT) deposited from polymer latex/SWCNT mixtures spin-coated at 2000 rpm. Information on the preparation and deposition of these polymer latex/CNT mixtures can be found in the SI, Section VII.

In Fig. 4, a large-area map of single-walled carbon nanotubes (SWCNTs) and methyl methacrylate/t-butyl acetate (MMA/t-BA) polymer latex particles covering an area of $(100\ \mu m)^2$ are displayed. The overall distribution of SWCNTs and polymer latex particles is inhomogeneous, as shown in Fig. 4a, b, c, e and f. The SWCNTs are mainly found inside (Fig. 4d, i, and l) and surrounding the latex particles (Fig. 4d), as well as in areas connecting the latex containing regions (Fig. 4g, h, j, and k). Additional images of locally occurring morphologies can be found in the SI, Section VIII, Figure S10. Hence, a web-like network of SWCNT's is formed that facilitates electrical conduction over macroscopic distances (mm to cm). While the alignment of the SWCNTs seems random over the web-like network at first sight, the electrical conductivity measured parallel to the spin-coating direction is actually 3 times higher ($\sim$120 S/m) than in the perpendicular direction ($\sim$40 S/m) [34]. These macroscopic measurements indicate that SWCNT alignment parallel to the spin coating direction occurs, most likely from the outward flow of the latex particles during spin-coating. To verify the preferential alignment of the SWCNT's with spin coating direction, we quantitatively analyzed the large area map.

In brief, quantification includes filtering and thresholding to isolate the SWCNT's from the background and latex particles, labeling of connected regions (SWCNT fragments) and determination of their orientation by measuring the angle between the SWCNT and spin-coating direction. Additional details on segmentation and quantification can be found in the Supporting information, SI, Section IX. Fig. 5 shows a polar plot displaying the distribution of the SWCNTs over the orientation angle illustrating the overall alignment of the SWCNTs with the spin-coating direction. The increase in angular count towards the extreme angles (i.e., 0°–10° and 170°–180°) indicates the global alignment, which is parallel to the spin-coating direction.

Here we emphasize again that if such measurements are carried out on areas/volumes smaller than the representative volume, the results will vary significantly as illustrated in Fig. 6. Fig. 6a shows a large-scale map of $(20\ \mu m)^2$ illustrating the preferential orientation of SWCNTs; however, a large-scale map of the same size (Fig. 6b) but located at a different position, shows a completely different morphology, in this case we can observe random orientation of the SWCNTs. Quantitative image analysis on Fig. 6a and b shows the significant difference in the alignment of SWCNTs (Fig. 7), which ultimately results in contradicting interpretations,

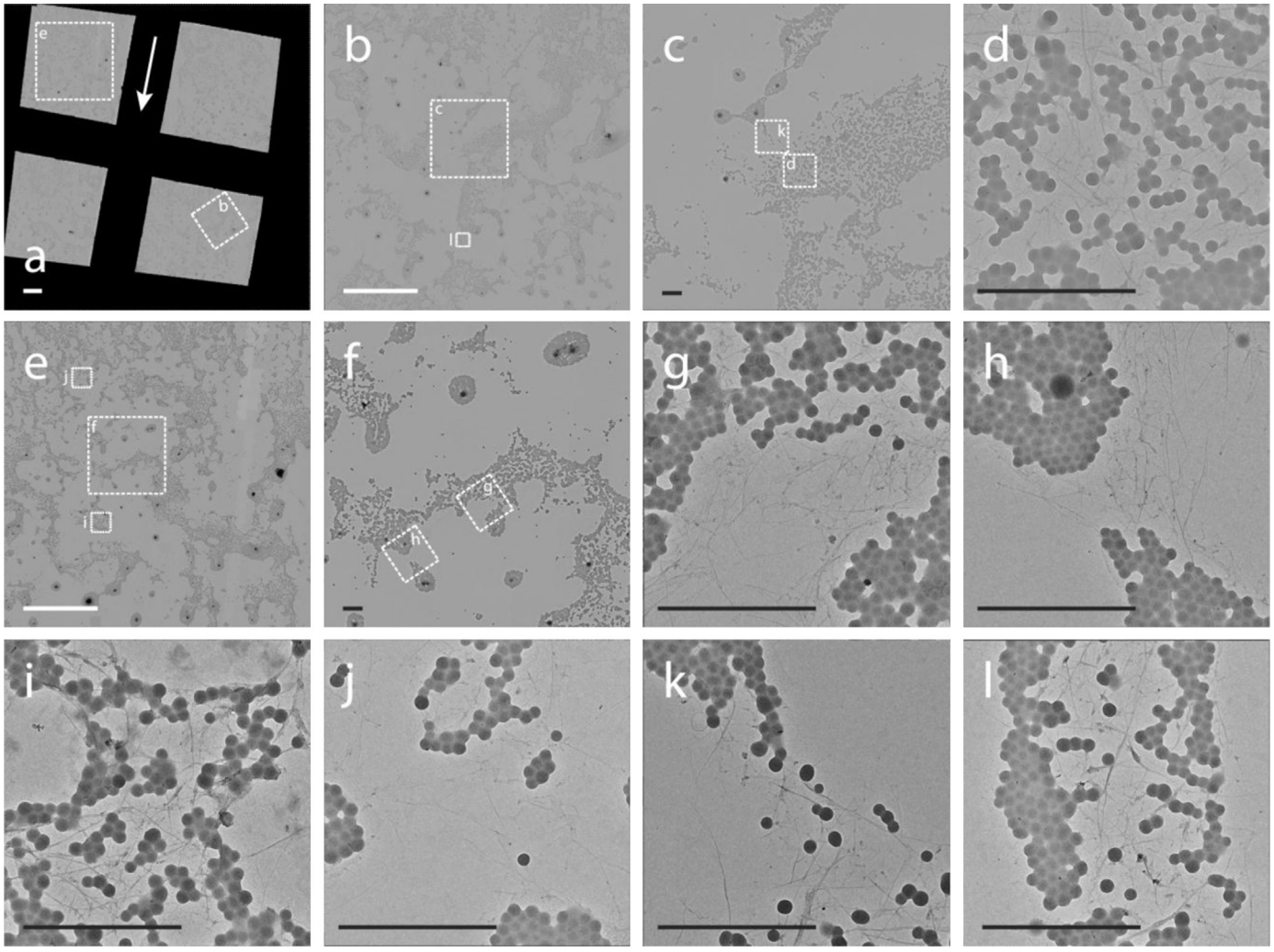

Fig. 4. Large-area BF-TEM map, illustrating the assembly of MMA/t-BA polymer latex-SWCNT over several length scales. The white arrow in Fig. 4a represents the direction parallel to spin-coating. The insets correspond to larger magnification images with the same label. White scale bars are 15 μm and black scale bars are 1 μm.

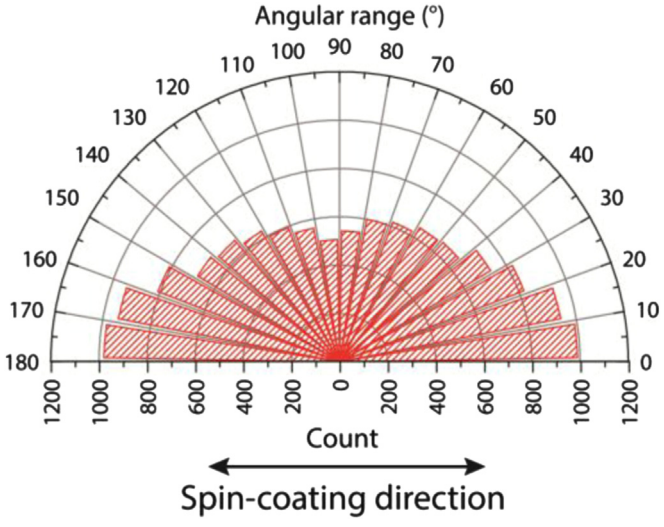

Fig. 5. Polar plot showing the distribution in orientation of SWCNTs. The distribution is summed-up values in 4 different meshes shown in Fig. 4a.

depending on the chosen area of imaging. The segmented images of Fig. 6 can be found in the SI, Section X. Now the question arises, whether or not the histogram shown in Fig. 5 is representative. In other words, what is the size of the representative area/volume? To extract the size of the representative volume, we carried out a histogram analysis as a function of area and results are presented in the SI, Section XI. This show that for areas larger than (48 k)^2 pixels, corresponding to 60^2 μm^2, results in virtually identical orientation distributions. The area analyzed (Fig. 5) is significantly larger than this minimum area (60^2 μm^2) and thus represents the orientation of SWCNTs accurately.

From the large-scale images and quantitative image analysis illustrated above, we conclude that the overall SWCNT alignment is tailored across three hierarchical orders of alignments of SWCNTs, namely (1) locally aligned SWCNTs (for several μm) in between the latex particles or in the boundaries of the latex particles connecting several latex containing regions (Figs. 4g and 4h), (2) mesoscale alignment of SWCNTs for several tens of μm (Fig. 6a) and (3) global SWCNT alignment along the spin-coating direction for several mm and cm (can be realized from the polar plot, Fig. 5). The frequency and distribution of this hierarchical ordering is controlled by the size and the size distribution of the SWCNTs and polymer latex particles as well as the fabrication conditions, like spin-coating speed and temperature. Obviously, the overall morphology ultimately determines the electrical conductivity [34].

7. Multi-layer co-extruded i-PP/HDPE polymer tapes

Multi-layer co-extrusion is a technique to fabricate multi-layer

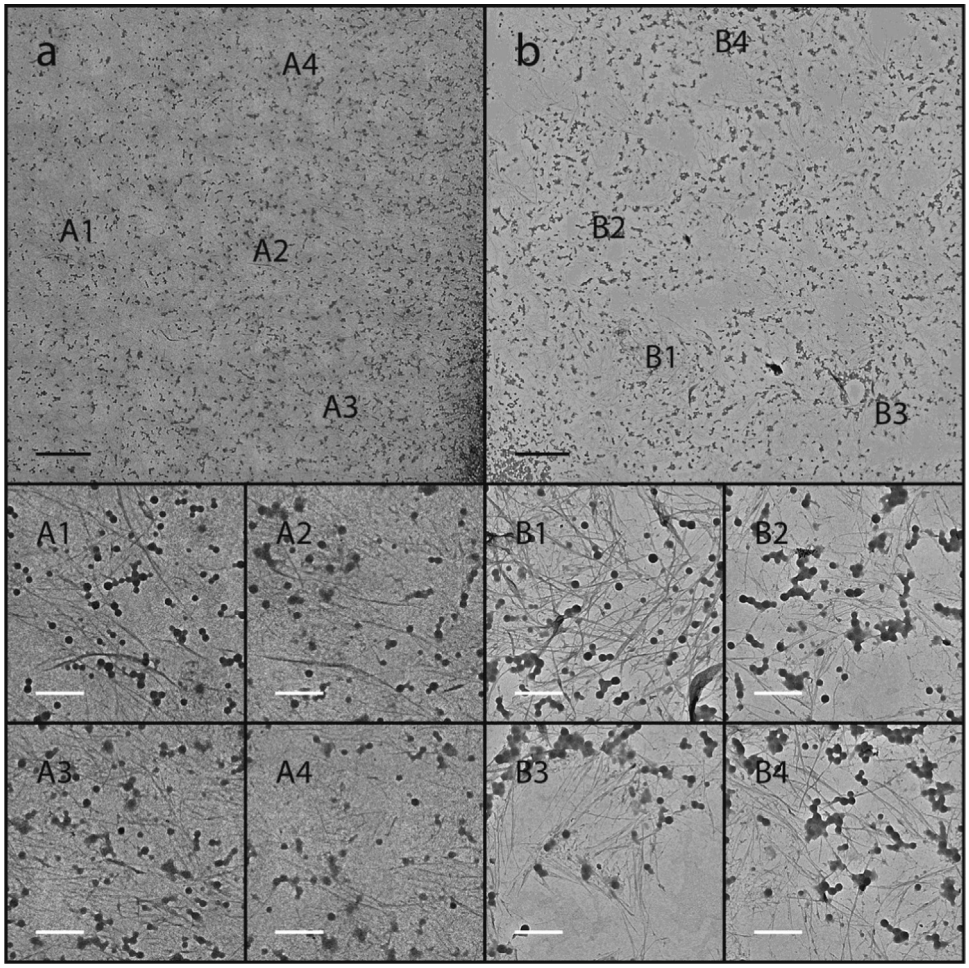

Fig. 6. Large-scale BF-TEM images illustrating (a) the aligned and (b) the almost randomly oriented SWCNTs. Black scale bars are 2 μm and white scale bars are 500 nm.

polymer tapes from tens to hundreds of micrometers in thickness composed of individual layers with thicknesses varying from ≈ 100 nm to several μm. Detailed information on the fabrication of such multi-layer polymer blends can be found in l′Abee et al. [1] and other references [35,36]. Multi-layer polymer tapes are utilized for food packaging and high-toughness materials on account of their excellent barrier properties such as low oxygen permeability. Gas transport occurs only/mainly through the amorphous regions between the crystalline lamellas introduced by processing. More precisely, lamellae orientation, i.e., perpendicular or parallel to the permeation direction, and the total amount of crystallinity as well as the resulting dimensions of the amorphous regions tune the film properties Furthermore, by proper designing the processing conditions, such as cooling speed, the number of layers, the layer thickness and the distance between layers, the amount of crystallinity and lamellae orientation within the phases can be controlled. For instance, in i-PP/HDPE (iso-tactic polypropylene/high-density polyethylene) multi-layer polymer blends, reducing the thickness of i-PP layer sandwiched between HDPE layers, induces confined crystallization of i-PP layers, which in-turn controls the gas permeability of the multilayer system [37]. The formation of such confined nanoscale morphologies throughout macroscale films is strongly influenced by the processing (film drawing) conditions, such as temperature and temperature

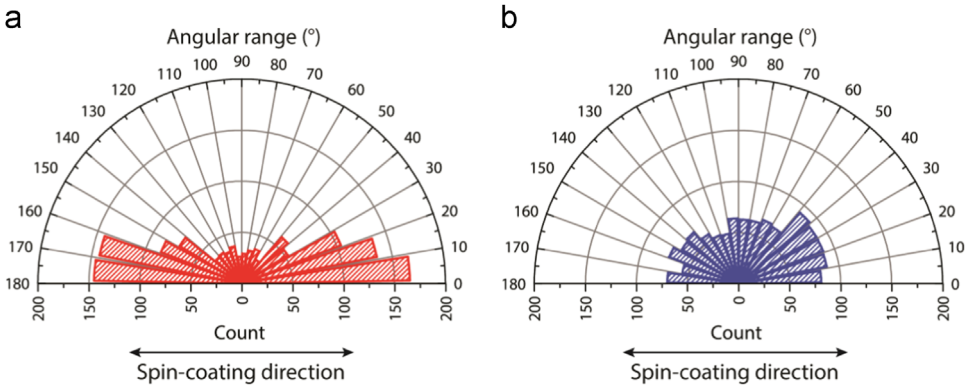

Fig. 7. Polar histogram illustrating the orientation distribution of SWCNTs in (a) an aligned region and (b) an almost randomly oriented region.

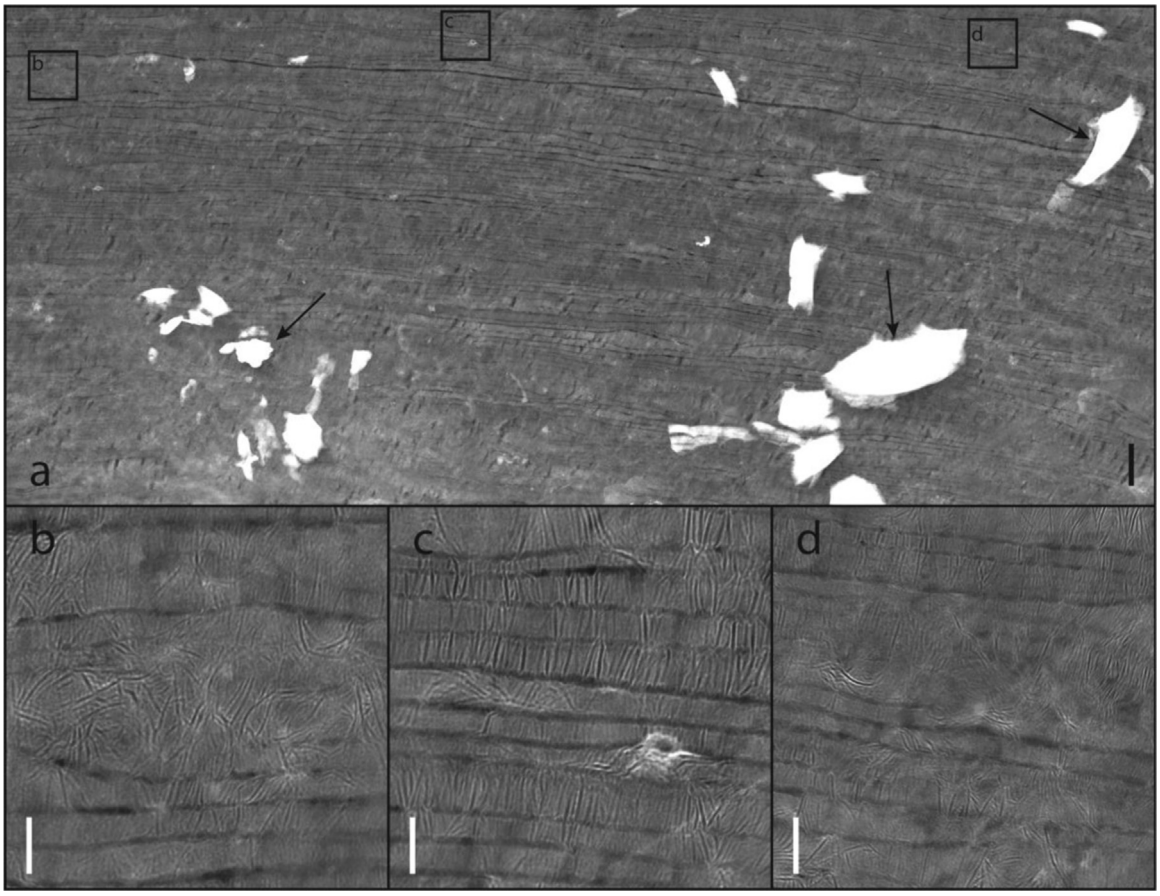

Fig. 8. (a) Large-scale STEM micrographs of 20/80 i-PP/HDPE multi-layers. White regions (marked in arrows) represents the debris accumulated during cutting; (b, c, d) Cut-outs showing the defects due to (b) flow instability and random HDPE lamella orientation, (c) non-uniformity in the layer thicknesses and change in orientation of the HDPE lamella, and (d) mixing of layers. Black scale bar is 1 μm and white scale bars are 200 nm.

gradients, and processing rate. Hence, morphological analysis of nanoscale features over mesoscopic to macroscopic length scale is a prerequisite for a better understanding of processing-structure-property relationships.

Fig. 8 shows a large-scale STEM map of 20/80 i-PP/HDPE multi-layers, where the light phase represents the HDPE layers and dark phase represents the i-PP layers. This multi-layer film was drawn at the rate of 1.5 m/min at 40 °C. Information on STEM imaging and EM sample preparation is given in the SI, Section XII. At first glance, we can notice that the layers are not straight. White regions (shown by arrows) in the large-scale map represents the debris scattered across the section from microtoming. Mesoscale variations, such as locally swollen HDPE layers (Fig. 8b), are noticed over the entire area of the sample. These defects in layers are caused by the flow instabilities during the processing, which in-turn results in non-uniform layer thicknesses and hence the distance between the layers also changes, as shown in Fig. 8c and d. These defects potentially disrupts the induced crystallinity and their presence results in localized random orientation of the crystalline phases (dark stripes in bright layers), as shown in Fig. 8b, and in mixing of layers, as shown in Fig. 8d. It should be noted that the image contrast is created by selective staining of the amorphous parts in the HDPE layers and assuming a homogeneous staining, a qualitative view on the amount of crystalline versus amorphous HDPE can be obtained from local intensity averages, apart from an analysis of the dark stripes resulting from an edge-on view of crystalline lamellae. The random orientation of the lamella in the localized defect regions is mainly induced by a slow cooling rate. Nevertheless, HDPE lamella have a predominant edge-on orientation (stacked perpendicular to the lateral side) in the defect-free regions, as shown in Fig. 8c. Because the HDPE lamella are thin, only a predominate edge-on orientation of *i*-PP lamella is observed. The presence of defects due to flow instabilities, such as layer thickness variability, disruption in the preferred orientation of lamella and localized mixing of layers, strongly indicates that the processing conditions and composition of multi-layers can further be optimized.

A 80/20 i-PP/HDPE multi-layer polymer tape drawn at the same rate and temperature (1.5 m/min at 40 °C) is shown in Fig. 9. Here we can notice that the layers are lying almost horizontal along the lateral direction throughout the lateral direction of the film while mixing of layers is not evident. Also here the mesoscale flow instability defects are noticed to be distributed throughout the large-scale map (Fig. 9c). Besides that, in some regions, layer thickness variations are also noticed over the width of the sample (Fig. 9d). The orientations of HDPE lamella are almost similar to those of the 20/80 i-PP/HDPE multi-layer sample; however, some cross-hatching (Fig. 9c) and localized flat-on orientation is noticed (shown by arrows in Fig. 9c and d). Because of the thin layers of HDPE lamella, the predominate edge-on orientation of *i*-PP lamella is also visible at several regions. Although qualitatively the 80/20 *i*-PP/HDPE multi-layer was observed to be better than the 20/80 i-PP/HDPE multi-layer, statistical information about these morphological features over the thickness and along the film plane are necessary to derive an optimum balance between layer composition, thickness, spacing, processing conditions and resulting barrier properties.

Quantitative image analysis was employed to reveal the statistical distribution of these structural features. Here we focused especially on the analysis of thickness and position of layers of 80/

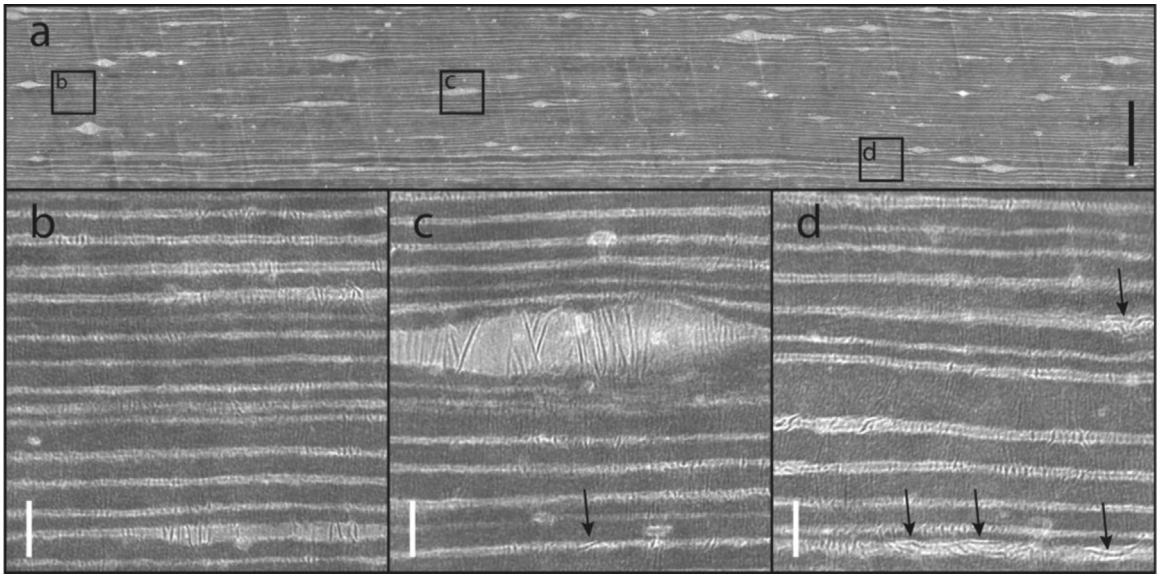

Fig. 9. (a) Large-scale STEM micrographs of 80/20 i-PP/HDPE multi-layers; (b, c, d) Cut-outs from Fig. 9a showing (b) a relatively uniform layer thicknesses and spacing, c) defects due to flow instability, (b) and (c) edge-on orientation of HDPE lamella and (d) non-uniformity in the layer thicknesses and flat-on orientation of HDPE lamella. Black scale bar is 1 μm and white scale bars are 200 nm.

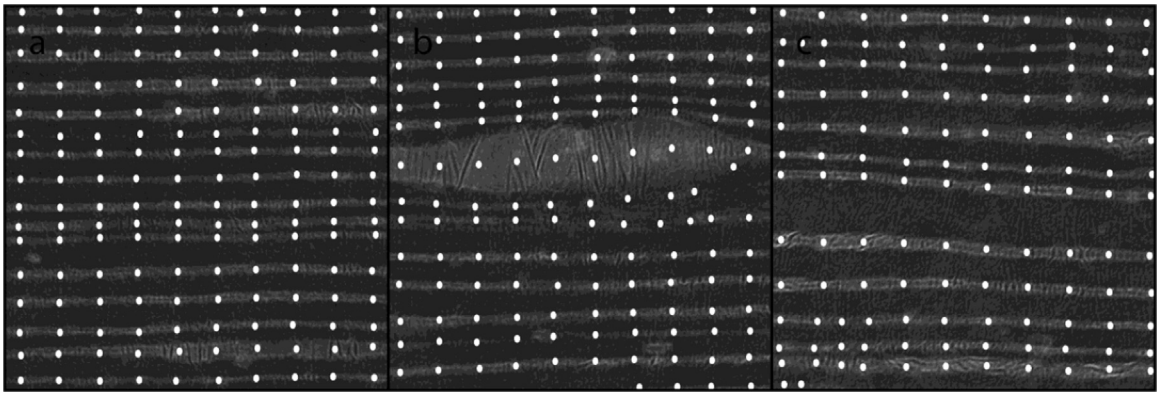

Fig. 10. Centroids (white dots) overlaid on the images for better illustration. Centroids were calculated for every 100 nm across the lateral side of the layers.

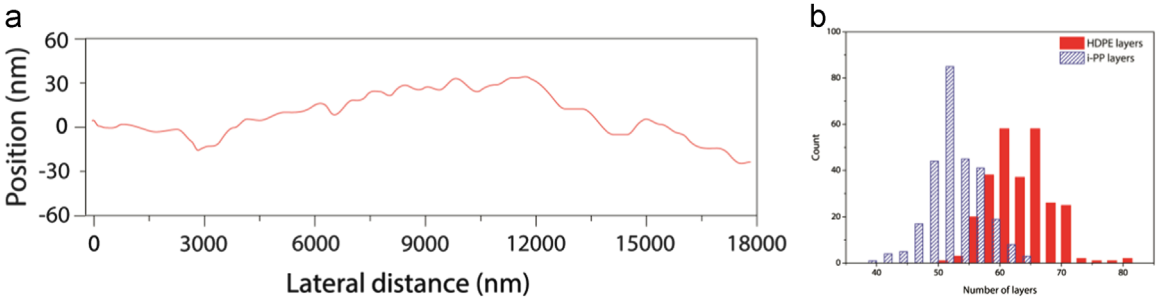

Fig. 11. (a) Centroids were connected along a HDPE layer over the complete large-area image gives information about the variation in the layer position; (b) Histogram showing the distribution of the number of HDPE and i-PP layers present along the width. Number of layers was measured at the interval of 100 pixels in lateral direction.

20 i-PP/HDPE multi-layer system to address the most obvious quality sign of processing, i.e., homogeneity of layering. We determined the position of each layer represented by centroids for every 100 nm along the tape direction. The details of the image analysis procedure are given in the SI, Section XIII. Briefly, quantification involves anisotropic Gaussian filtering to smear-out the crystallites, which aids the segmentation process and also to suppress the effects of STEM scanning lines, segmentation by Otsu-thresholding, and morphological closing operations followed by determination of the local centroids. In Fig. 10, we displayed the measured centroids representing the HDPE layers shown in Fig. 9b–d. For better understanding we overlaid the centroids on the top of the image. The centroids measured for the complete large-scale STEM map are shown in Figure S15. By appropriate analysis of centroids, we can track the defect zones, which leads to the regions with potential change in morphologies. For instance, by connecting the subsequent centroids along the width of the same layer, the waviness and continuity of the layers is obtained as shown in Fig. 11a. Although qualitatively the layers are observed to be rather uniform and continuous, the quantitative analysis

reveals the significant waviness in layers, which is inaccessible by visual qualitative analysis, which also suggests the massive variation in thicknesses of layers. These thickness variations can be tracked by extending the above procedure to all the layers (both HDPE and i-PP layers) along the transverse direction. Illustration of such connected centroids along the width of all the layers results in an incomprehensible graph; hence, in Figure S16, we have shown such connected centroids in 3 dimensions illustrating the waviness of subsequent HDPE layers for the cut-outs shown in Fig. 9. By measuring the distance between the 2 subsequent HDPE centroids in transverse direction, the local thickness of i-PP layer can be determined and vice-versa. Any increase or decrease in thickness from the expected thickness shows the defect zone. Besides that, the intensity of the defects from one end to another end (transverse direction) can be identified by measuring the average distance between subsequent layers as shown in Figure S17. The peaks (shown by arrows in Figure S17) represents the strong localized defect region in multi-layers. The above analysis also yields information about the distribution in number of HDPE and i-PP layers along the width of the sample as shown in Fig. 11b. This analysis reveals that, although the multi-layer fabrication technique was intended to fabricate same number of sandwiched HDPE and i-PP layers, it was not achieved over the entire sample and shows the potential change in the crystallite orientations across the sample. DSC measurements reveals 38% and 47% of crystallinity in the *i*-PP and HDPE phases, respectively. Visually we notice that~50% of the area is occupied by dark stripes in the HDPE layers. Although this observation matches approximately with the DSC measurements, as mentioned, we cannot obtain conclusive results from a 2D analysis of a 3D morphology. Quantification of area fraction of HDPE resulted 32% HDPE, to be compared with 20% nominally. This increase in HDPE content is mainly due to flow instability defects (locally swollen HDPE along a layer) that are distributed throughout the sample. These localized increases in the amount of HDPE apparently increases the overall area fraction in the segmented image.

8. Conclusions and outlook

We have shown that quantitative nanoscopy (large-scale (S) TEM imaging, stitching and quantification) is a powerful technique well-suited for the quantitative analysis of polymers and composites that are structured over multiple length scales. This methodology renders electron microscopy to be closer to becoming a bulk characterization tool and allows an appealing bottom-up understanding of multi-scale assembly to material properties. To that purpose a versatile, large-scale EM imaging toolbox (*TU/e Acquisition ToolBox*) was developed, in which imaging can be performed both in STEM as well as in TEM mode together with an independent stitching module to stitch acquired EM images (*TU/e Stitcher*). The *TU/e Acquisition ToolBox* and *TU/e Stitcher* can be downloaded from: http://sourceforge.net/projects/tue-acquisition-toolbox/. We illustrated the power of such an analysis by examining two multi-scale morphologies over a much larger length scale than conventionally performed. For the spin-coated polymer latex-SWCNT composite, the analysis revealed the presence of three-tier hierarchical length scale morphology, including oriented and non-oriented SWCNT areas. For the multi-layer co-extruded i-PP/HDPE polymer tapes, the analysis indicated the presence of several types of defects, of which the amount and spatial distribution could be quantitatively assessed. For both cases it is unlikely that conventional analysis would have discovered the features indicated.

Acknowledgments

The research leading to these results has received funding from the European Union Seventh Framework Programme (FP7-MC-ITN) under Grant agreement no. 264710. The authors would like to thank the Directorate-General for Science, Research and Development of the European Commission for financial support of the research, Seyno Sluyterman, Andreas Voigt, Tomas Molina, and Max Otten (FEI Company, the Netherlands) for their support and thoughtful discussions on the development of the automation toolbox (*TU/e Acquisition ToolBox*), Anne Spoelstra (Eindhoven University of Technology) for her help in microtoming the multi-layer polymer tapes. The authors would also like to thank Mohammed Moradi, and Alex van Herk for providing TEM samples of spin-coated polymer latex-SWCNT mixture, and Han Goossens for providing the multi-layer polymer tapes samples.

Appendix A. Supplementary material

Supplementary data associated with this article can be found in the online version at http://dx.doi.org/10.1016/j.ultramic.2015.10.004.

References

[1] R.M. l'Abee, A.M. Vissers, J.G. Goossens, A.B. Spoelstra, M. van Duin, Characterization of the morphology of co-extruded, thermoplastic/rubber multi-layer tapes, Anal. Chim. Acta 654 (2009) 11–19.
[2] E. Tkalya, M. Ghislandi, A. Alekseev, C. Koning, J. Loos, Latex-based concept for the preparation of graphene-based polymer nanocomposites, J. Mater. Chem. 20 (2010) 3035–3039.
[3] R. Ishige, T. Higuchi, X. Jiang, K. Mita, H. Ogawa, H. Yokoyama, A. Takahara, H. Jinnai, Structural Analysis of microphase separated interface in an ABC-type triblock terpolymer by combining methods of synchrotron-radiation grazing incidence small-angle X-ray scattering and electron microtomography, Macromolecules 48 (2015) 2697–2705.
[4] C.J. Gommes, H. Friedrich, M. Wolters, P.E. de Jongh, K.P. de Jong, 2-Point correlation function of nanostructured materials via the grey-tone correlation function of electron tomograms: a three-dimensional structural analysis of ordered mesoporous silica, Acta Mater. 58 (2010) 770–780.
[5] G.H. Michler, Study of structure-property correlations in polymers by techniques of electron-microscopy, Phys. Status Solidi (a) Appl. Res. 150 (1995) 185–200.
[6] L.F. Kourkoutis, J.M. Plitzko, W. Baumeister, Electron microscopy of biological materials at the nanometer scale, Annu. Rev. Mater. Res. 42 (2012) 33–58.
[7] H. Friedrich, P.M. Frederik, G. de With, N.A. Sommerdijk, Imaging of self-assembled structures: interpretation of TEM and cryo-TEM images, Angew. Chem. 49 (2010) 7850–7858.
[8] P. Krishnamachari, R. Hashaikeh, M. Tiner, Modified cellulose morphologies and its composites; SEM and TEM analysis, Micron 42 (2011) 751–761.
[9] K. Gnanasekaran, G. de With, H. Friedrich, On packing, connectivity, and conductivity in mesoscale networks of polydisperse multiwalled carbon nanotubes, J. Phys. Chem. C 118 (2014) 29796–29803.
[10] D.D. Bock, W.C.A. Lee, A.M. Kerlin, M.L. Andermann, G. Hood, A.W. Wetzel, S. Yurgenson, E.R. Soucy, H.S. Kim, R.C. Reid, Network anatomy and in vivo physiology of visual cortical neurons, Nature 471 (2011) 177 , U159.
[11] K. Lu, E. Sourty, J. Loos, Annular dark-field scanning transmission electron microscopy (ADF-STEM) tomography of polymer systems, J. Electron Microsc. 59 (2010) S39–S44.
[12] K. Aoyama, T. Takagi, A. Hirase, A. Miyazawa, STEM tomography for thick biological specimens, Ultramicroscopy 109 (2008) 70–80.
[13] S. Motoki, T. Kaneko, Y. Aoyama, H. Nishioka, Y. Okura, Y. Kondo, H. Jinnai, Dependence of beam broadening on detection angle in scanning transmission electron microtomography, J. Electron Microsc. 59 (2010) S45–S53.
[14] J. Loos, E. Sourty, K. Lu, B. Freitag, D. Tang, D. Wall, Electron tomography on micrometer-thick specimens with nanometer resolution, Nano Lett. 9 (2009) 1704–1708..
[15] S. Nickell, F. Forster, A. Linaroudis, W.D. Net, F. Beck, R. Hegerl, W. Baumeister, J.M. Plitzko, TOM software toolbox: acquisition and analysis for electron tomography, J. Struct. Biol., 149, (2005) 227–234.
[16] D.N. Mastronarde, Automated electron microscope tomography using robust prediction of specimen movements, J. Struct. Biol. 152 (2005) 36–51.
[17] C. Suloway, J. Shi, A. Cheng, J. Pulokas, B. Carragher, C.S. Potter, S.Q. Zheng, D. A. Agard, G.J. Jensen, Fully automated, sequential tilt-series acquisition with Leginon, J. Struct. Biol. 167 (2009) 11–18.

[18] N. Kisseberth, M. Whittaker, D. Weber, C.S. Potter, B. Carragher, emScope: a tool kit for control and automation of a remote electron microscope, J. Struct. Biol. 120 (1997) 309–319.
[19] J.L. Lei, J. Frank, Automated acquisition of cryo-electron micrographs for single particle reconstruction on an FEI Tecnai electron microscope, J. Struct. Biol. 150 (2005) 69–80.
[20] F.G. Faas, M.C. Avramut, B.M. van den Berg, A.M. Mommaas, A.J. Koster, R. B. Ravelli, Virtual nanoscopy: generation of ultra-large high resolution electron microscopy maps, J. Cell Biol. 198 (2012) 457–469.
[21] J.R. Anderson, B.W. Jones, J.H. Yang, M.V. Shaw, C.B. Watt, P. Koshevoy, J. Spaltenstein, E. Jurrus, U.V. Kannan, R.T. Whitaker, D. Mastronarde, T. Tasdizen, R.E. Marc, A computational framework for ultrastructural mapping of neural circuitry, Plos Biol. 7 (2009) 493–512.
[22] D. Wolf, A. Lubk, H. Lichte, H. Friedrich, Towards automated electron holographic tomography for 3D mapping of electrostatic potentials, Ultramicroscopy 110 (2010) 390–399.
[23] S. Preibisch, S. Saalfeld, P. Tomancak, Globally optimal stitching of tiled 3D microscopic image acquisitions, Bioinformatics 25 (2009) 1463–1465.
[24] J. Schindelin, I. Arganda-Carreras, E. Frise, V. Kaynig, M. Longair, T. Pietzsch, S. Preibisch, C. Rueden, S. Saalfeld, B. Schmid, J.Y. Tinevez, D.J. White, V. Hartenstein, K. Eliceiri, P. Tomancak, A. Cardona, Fiji: an open-source platform for biological-image analysis, Nat. Method. 9 (2012) 676–682.
[25] B.E. McKenzie, H. Friedrich, M.J.M. Wirix, J.F. de Visser, O.R. Monaghan, P.H. H. Bomans, F. Nudelman, S.J. Holder, N.A.J.M. Sommerdijk, Controlling internal pore sizes in bicontinuous polymeric nanospheres, Angew. Chem. 54 (2015) 2457–2461.
[26] I. Vukovic, H. Friedrich, D.H. Merino, G. Portale, G. ten Brinke, K. Loos, Shear-Induced Orientation of Gyroid PS-b-P4VP(PDP) Supramolecules, Macromol. Rapid Commun. 34 (2013) 1208–1212.
[27] H. Jinnai, X. Jiang, Electron tomography in soft materials, Curr. Opin. Solid State Mater. Sci. 17 (2013) 135–142.
[28] N. Kawase, M. Kato, H. Nishioka, H. Jinnai, Transmission electron microtomography without the “missing wedge” for quantitative structural analysis, Ultramicroscopy 107 (2007) 8–15.
[29] A.V. Kyrylyuk, M.C. Hermant, T. Schilling, B. Klumperman, C.E. Koning, P. van der Schoot, Controlling electrical percolation in multicomponent carbon nanotube dispersions, Nat. Nano 6 (2011) 364–369.
[30] N. Grossiord, J. Loos, L. van Laake, M. Maugey, C. Zakri, C.E. Koning, A.J. Hart, High-conductivity polymer nanocomposites obtained by tailoring the characteristics of carbon nanotube fillers, Adv. Funct. Mater. 18 (2008) 3226–3234.
[31] M.C. Hermant, B. Klumperman, A.V. Kyrylyuk, P. van der Schoot, C.E. Koning, Lowering the percolation threshold of single-walled carbon nanotubes using polystyrene/poly(3,4-ethylenedioxythiophene): poly(styrene sulfonate) blends, Soft Matter 5 (2009) 878–885.
[32] A. Wysocki, H. Lowen, Oscillatory driven colloidal binary mixtures: axial segregation versus laning, Phys. Rev. E 79 (2009) 041408-1–041408-5.
[33] D.T.W. Toolan, R. Hodgkinson, J.R. Howse, Stroboscopic microscopy-direct imaging of structure development and phase separation during spin-coating, J. Polym. Sci.: Polym. Phys. 52 (2014) 17–25.
[34] M.-A. Moradi, K.L. Angoitia, S. van Berkel, K. Gnanasekaran, H. Friedrich, J.P.A. Heuts, P.P.A.M. van der Schoot, A.M. van Herk, Submitted to Langmuir (under review).
[35] J.C. van der Hoeven, R. Wimberger-Friedl, H.E.H. Meijer, Homogeneity of multilayers produced with a static mixer, Polym. Eng. Sci. 41 (2001) 32–42.
[36] C.D. Mueller, S. Nazarenko, T. Ebeling, T.L. Schuman, A. Hiltner, E. Baer, Novel structures by microlayer coextrusion-Talc-filled PP, PC/SAN, and HDPE/LLDPE, Polym. Eng. Sci. 37 (1997) 355–362.
[37] J.M. Carr, D.S. Langhe, M.T. Ponting, A. Hiltner, E. Baer, Confined crystallization in polymer nanolayered films: a review, J. Mater. Res. 27 (2012) 1326–1350.